Article

Excellent Adsorption of Dyes via MgTiO$_3$@g-C$_3$N$_4$ Nanohybrid: Construction, Description and Adsorption Mechanism

Abueliz Modwi [1], Mohamed R. Elamin [2,*], Hajo Idriss [3], Nuha Y. Elamin [2], Fatima A. Adam [2], Abuzar E. Albadri [4] and Babiker Y. Abdulkhair [2,5,*]

[1] Department of Chemistry, College of Science and Arts, Qassim University, Ar Rass 52571, Saudi Arabia
[2] Chemistry Department, College of Science, Imam Mohammad Ibn Saud Islamic University (IMSIU), Riyadh 11623, Saudi Arabia
[3] Physics Department, College of Science, Imam Mohammad Ibn Saud Islamic University (IMSIU), Riyadh 13318, Saudi Arabia
[4] Department of Chemistry-Buraydah Almolaydah, College of Science, Qassim University, Buraydah 51452, Saudi Arabia
[5] Chemistry Department, Faculty of Science, Sudan University of Science and Technology (SUST), Khartoum P.O. Box 13311, Sudan
* Correspondence: mrabuzaid@imamu.edu.sa (M.R.E.); byabdulkhair@imamu.edu.sa or babiker35.by@gmail.com (B.Y.A.); Tel.: +96-65-0798-4498 (M.R.E.)

Abstract: This report investigates the elimination of hazardous Rhodamine B dye (RhB) from an aqueous medium utilizing MgTiO$_3$@g-C$_3$N$_4$ nanohybrids manufactured using a facile method. The nanohybrid MgTiO$_3$@g-C$_3$N$_4$ was generated using an ultrasonic approach in the alcoholic solvent. Various techniques, including HRTEM, EDX, XRD, BET, and FTIR, were employed to describe the fabricated MgTiO3@g-C3N4 nanohybrids. RhB elimination was investigated utilizing batch mode studies, and the maximum removal was attained at pH 7.0. The RhB adsorption process is more consistent with the Langmuir isotherm model. The highest adsorption capacity of MgTiO$_3$@g-C$_3$N$_4$ nanohybrids for RhB was determined to be 232 mg/g. The dye adsorption followed a pseudo-second-order model, and the parameters calculated indicated that the kinetic adsorption process was spontaneous. Using ethanol and water, the reusability of the nanomaterial was investigated, and based on the results; it can be concluded that the MgTiO$_3$@g-C$_3$N$_4$ nanohybrids are easily regenerated for dye removal. The removal mechanism for the removal of RhB dye into MgTiO$_3$@g-C$_3$N$_4$ nanohybrids was also investigated.

Keywords: MgTiO$_3$@g-C$_3$N$_4$ nanohybrid; RhB dye uptake; adsorption modeling; removal mechanism

1. Introduction

The continuous expansion of the industrial sector has resulted in a dramatic increase in wastewater production [1,2]. Dyes are commonly found in effluent due to their extensive usage in the packaging, woven, leather, cosmetics, and food industries [3–5]. Synthetic dyes display substantial mutagenic and cancerous consequences [6–8]. Rhodamine B (RhB) dye is an artificial colorant frequently utilized to decorate fabrics and food items. It is an organic fluorescent pigment that is brilliant red and is employed as a coloring agent in various sectors, including fabrics, paper, paint, and others. It is a widely utilized pigment in many sectors due to its excellent water solubility and inexpensive cost [9–12]. However, colors cannot be biodegraded because they have intricate chemical structures. RhB dye is resistant to sunlight, fire, and oxidation like other dyes and is not biodegradable [13,14]. According to several research studies, RhB dye is mutagenic and carcinogenic to humans and animals. It produces biological problems such as rashes on the skin, lung irritation, hemolysis, and deteriorating liver and renal functions [15–17]. Since it is employed as a water-monitoring system to measure the flow rates and directions, it is known as a

luminous water tracer [18,19]. Cleaning up dyes in wastewater before dumping them into the environment is vital in preventing potential health problems and environmental harm. Many years of research on dye elimination from industrial wastewater have been conducted. Decolorization of water can be accomplished by oxidation, adsorption, or filtration, and different technological processes [20,21]. Removing dye from water by adsorption methods is one of the most successful techniques. Therefore, the alienation of pigments using adsorption onto zeolite, charcoal, sand, agricultural residues, activated carbon, and slag has been studied, and the adsorption isotherm was appropriately examined [22,23]. These adsorption techniques extract pigments from concentrated industrial waste [24–27]. However, the regeneration of most adsorptive materials is challenging for some of these adsorbents. In addition, the cost of adsorption procedures employing such materials is high. Nowadays, nanotechnology is one of the most remarkable technologies for effectively eliminating dye from sewage with adsorption approaches [28,29]. This technology is useful for dealing with water containing small amounts of organic and inorganic dyes, and it is a low cost compared to other methods. Recently, the most efficient adsorption and photocatalytic agents for entirely removing dyes from sewage are nanoparticles and nanocomposites [30,31]. Notably, the features of oxide nanocrystals such as MgO, TiO_2, ZnO, and CuO are widely employed in pollutant removal due to their unique physicochemical functions, which may also be modified by doping with other materials to meet specific needs and usage [4,32].

Graphitic carbon nitride (g-C_3N_4), one of the essential double-layered materials, has garnered global interest in multiple disciplines, such as photocatalytic degradation, energy conversion, and ecological environment protection [32–34]. There has been much interest in compounds derived from g-C_3N_4 due to their unique qualities, including physicochemical stability, low cost, and low environmental impact [35,36]. The current work aims to develop a low-cost, high-performance g-C_3N_4-based metallic nanocomposite for dye eradication in the aquatic phase. This research contributes significantly to the g-C_3N_4 structural design and property modulation via double doping by MgO and TiO_2.
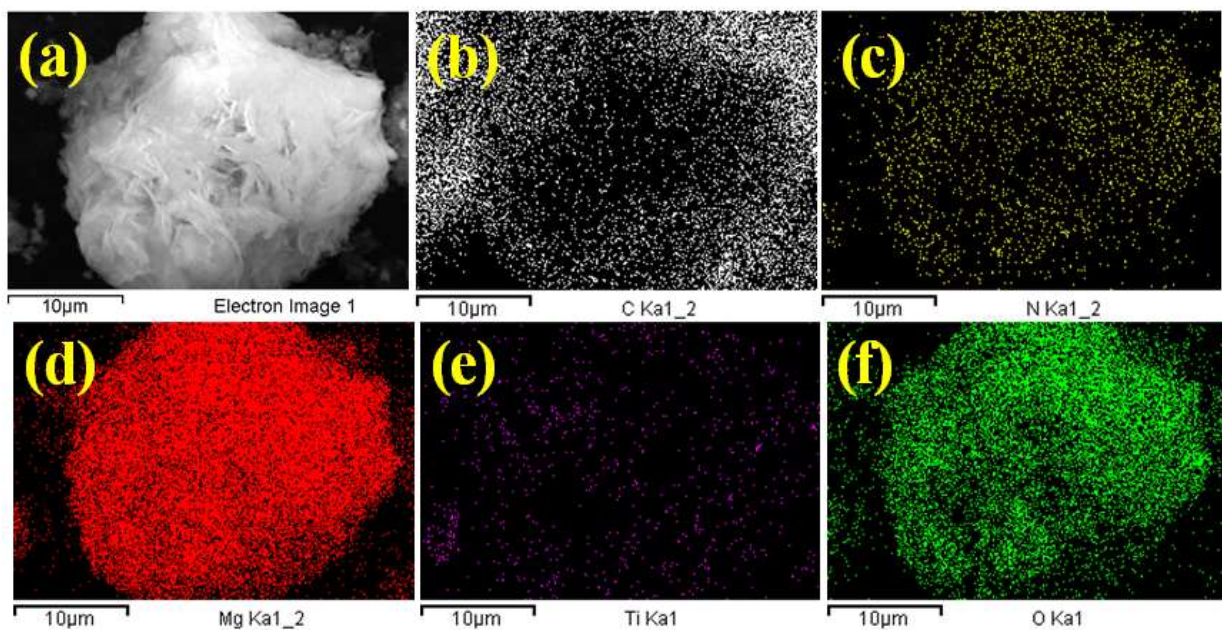
2. Results and Discussion

2.1. MgTiO$_3$@g-C$_3$N$_4$ Nanohybrids Structure Characteristics

The as-fabricated $MgTiO_3$@g-C_3N_4 nanohybrid was analyzed by transmission electron microscopy (TEM). As shown in Figure 1a–c, the as-synthesized $MgTiO_3$@g-C_3N_4 nanohybrids exhibited characteristic 2D nanosheet-like nanoparticle architectures with a corrugated thickness of around 30 nm. The average diameter of the MgO and TiO_3 nanoparticles integrated into the $MgTiO_3$@g-C_3N_4 nanohybrid composite is less than 20 nm. $MgTiO_3$ nanoparticles are disseminated well on the surface of g-C_3N_4 which generates an abundance of self-active sites on the surface of $MgTiO_3$@g-C_3N_4 nanohybrids. The Energy-Dispersive-X-ray Spectroscopy (EDX) image identifies the constituents of the $MgTiO_3$@g-C_3N_4 sorbent material. Therefore, it is evident from the results of Energy-Dispersive-X-ray Spectroscopy of $MgTiO_3$@g-C_3N_4 nanohybrids that the surface consists of magnesium (Mg), titanium (Ti), oxygen (O), nitrogen (N), and carbon (C), as the spectrum corresponds to these constituents, which are described in Figure 1d.

The presence of magnesium and titanium can determine the development of the combination of nanohybrid and oxygen in addition to carbon and nitrogen (Figure 2a–f). The EDS elemental mapping (Figure 2) displays the elemental maps of the composite constituents N, C, O, Mg, and Ti along with the appropriate overlay image. In order to ensure even distribution throughout the composite, the contrast between dark and light colors is used.
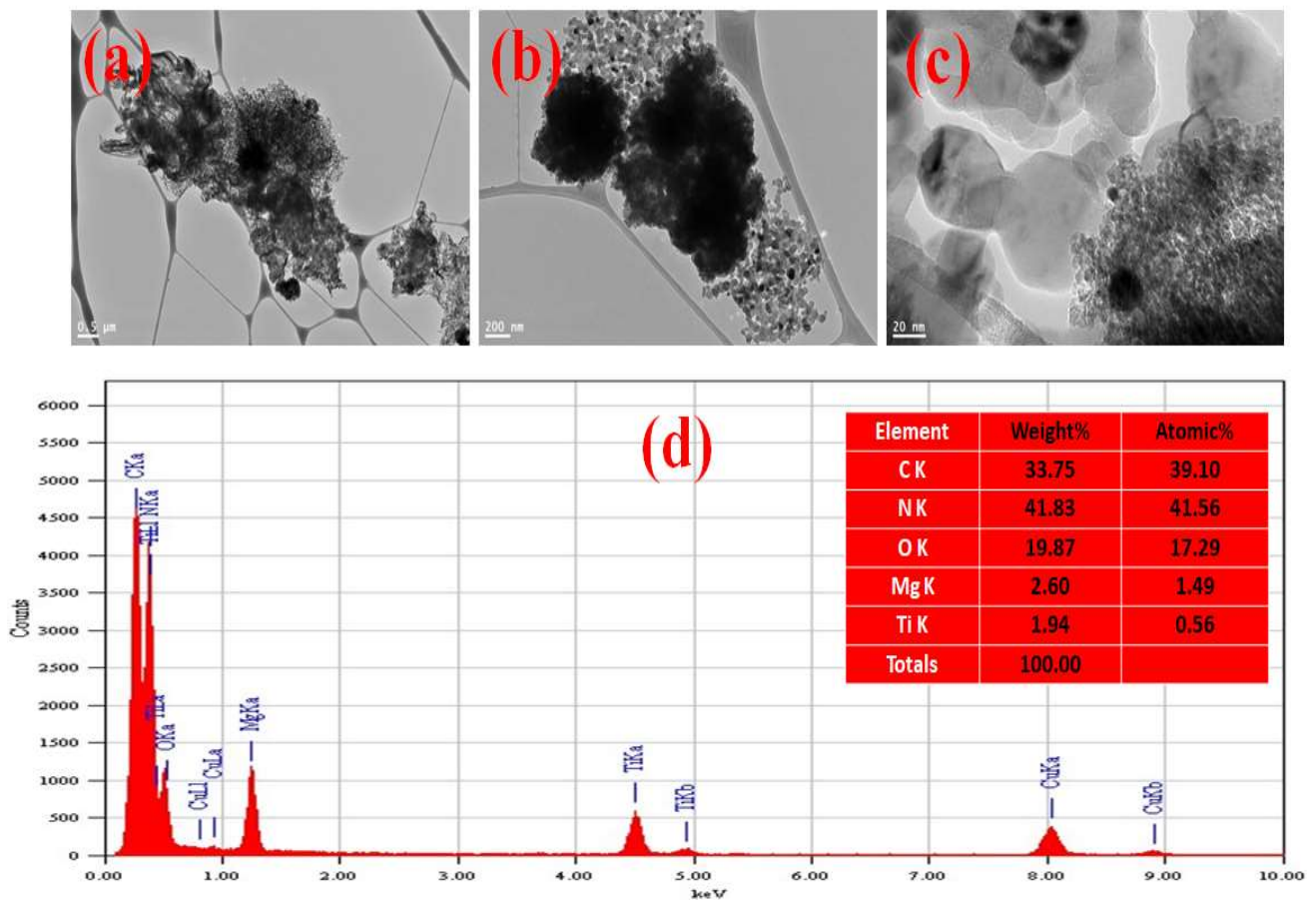
Figure 1. (**a**–**c**) TEM results of MgTiO$_3$@g-C$_3$N$_4$ nanohybrids from different spots; (**d**) EDS obtaining for the synthesized MgTiO$_3$@g-C$_3$N$_4$ nanohybrids.

Element	Weight%	Atomic%
C K	33.75	39.10
N K	41.83	41.56
O K	19.87	17.29
Mg K	2.60	1.49
Ti K	1.94	0.56
Totals	100.00	

Figure 2. (**a**) EDS electronic image of MgTiO$_3$@g-C$_3$N$_4$ nanohybrid; elemental mapping of (**b**) carbon, (**c**) nitrogen, (**d**) magnesium, (**e**) titanium, and (**f**) oxygen in the synthesized MgTiO$_3$@g-C$_3$N$_4$ nanohybrids.

The XRD spectra of the $MgTiO_3$@g-C_3N_4 nanohybrids, which can be seen in Figure 3a, exhibit well-defined diffraction peaks with relative broadening and intensity, demonstrating the creation of a well-nanocrystallized phase(s). The identification of the peaks through the use of the High Score algorithm reveals the existence of three phases, specifically MgO, anatase TiO_2, and g-C_3N_4. It would appear that the typical diffraction peaks for g-C_3N_4 are located at $2\theta = 12.7°$ and $27.38°$. These peaks appear to match the in-plane structural stacking pattern (100) and the interlayer layering plane (002) of the hexagonal structure (JCPDS card No. 87-1526) [37]. In comparison, the peaks that are placed at 2θ of $25.07°$, $37.59°$, $47.05°$, $53.91°$, $61.99°$, $69.09°$, and $74.53°$ indicate the characteristic reflections (101), (004), (200), (105), (204), (116), and (220) of the anatase phase TiO_2 (JCPDS card No. 021-1272) [38]. The additional peaks that were detected at 2θ angles of $36.61°$, $42.53°$, $61.99°$, and $78.16°$ have been ascribed to the (111), (200), (220), and (222) planes of the MgO cubic structure [39].
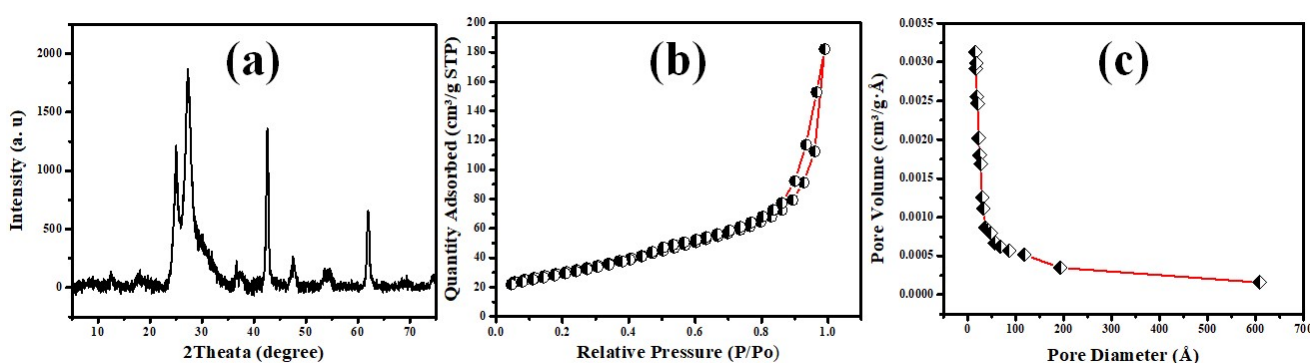
**Figure 3.** (**a**) XRD pattern, (**b**) the hysteresis loop, and (**c**) pore diameter distribution results of $MgTiO_3$@g-C_3N_4 nanohybrid.

Figure 3b displays the surface area and pore particle diameter characteristics of the nanohybrid $MgTiO_3$@g-C_3N_4 as manufactured. The adsorption-desorption graphs of $MgTiO_3$@g-C_3N_4 nanohybrid suited isotherm type IV and produced a hysteresis loop (H2) at relative pressures between 0.0 and 1.0. (Figure 3b). This result validated the mesoporous nature of the as-prepared $MgTiO_3$@g-C_3N_4 nanohybrid [40–42], which was further corroborated by the pore size distribution map generated using the Barret-Joyner-Halender (BJH) method. The enhanced surface area and porosity of the $MgTiO_3$@g-C_3N_4 nanohybrid, as revealed by a bigger specific surface area and a higher pore volume, will increase the adsorption capacity due to the presence of additional active sites on the surface [42]. In addition, the $MgTiO_3$@g-C_3N_4 nanohybrid isotherm exhibits a substantial BET surface area (S_{BET}) of $107 \text{ m}^2 \cdot \text{g}^{-1}$. In addition to its high surface area, the mesoporous structure of $MgTiO_3$@g-C_3N_4 nanohybrid makes it a promising candidate for metal ion and organic pollutant adsorption by providing a large number of active sites. The pore size distribution plot (Figure 3c) displays a mean pore diameter of 15.75 nm and a cumulative pore volume of $0.254 \text{ cm}^3 \text{ g}^{-1}$ due to BJH adsorption.

2.2. Adsorption Studies

2.2.1. Effect of Initial Concentration and pH Changing

In order to determine the influence of initial dye concentration on adsorption, the beginning concentration was varied from 5.0 to 100.0 mg/L (Figure 4a). The adsorption capacity of RhB increases from 18.5 to 215 mg/g as the initial concentration of RhB increases. With a higher initial dye concentration, the gradient of dye molecules increases, resulting in a greater adsorption capacity of $MgTiO_3$@g-C_3N_4 nanohybrid. As the concentration of the dye increases, the number of dye molecules in the solution will exceed the number of reactive sites on the composite's surface. Due to their rising repulsion, the $MgTiO_3$@g-C_3N_4 nanohybrid will become saturated with dye molecules, decreasing dye adsorption.
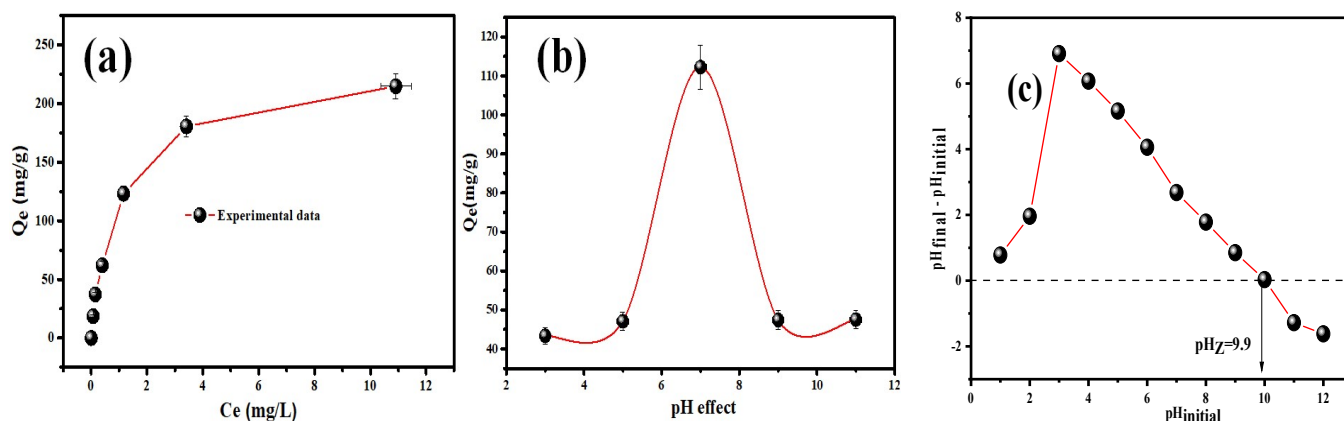
Figure 4. (**a**) Impact of initial fed concentration, (**b**) Effect of solution pH on adsorption of RhB by MgTiO3@g-C3N4 nanohybrid from 50 mg L^{-1} using 10 mg sorbent at 25 °C, and (**c**) the zero-charge investigation.

Figure 4b depicts the influence of pH on the RhB sorption onto $MgTiO_3@g\text{-}C_3N_4$. Furthermore, the removal effectiveness of $MgTiO_3@g\text{-}C_3N_4$ exceeded 90% of RhB at a pH of 7.0. In addition, it can be noted that in both acidic and alkaline media (pH $\geq$ 5.0 and pH $\leq$ 9.0), the removal efficiency decreased dramatically.

Metal oxides are recognized for their amphoteric activity in aqueous solutions; thus, MgO and TiO2 in the nanocomposite may react with either H^+ or ^-OH ions [43,44]. The pH drift method was employed to determine the point of zero charge P_{ZC} of $MgTiO_3@g\text{-}C_3N_4$ nanocomposite. Figure 4c demonstrates that the P_{ZC} was located at PH = 9.9 where no electrostatic attraction will occur; on the other hand, below this PH the MgTiO3@g-C3N4 surface will be positively-charged and favors the sorption of negatively-charged species [45,46].

### 2.2.2. The Impact of Equilibrium Contacts Time and Adsorption Kinetic Studies

Contact durations up to 120 min were investigated for their influence on RhB adsorption capacity. As shown in Figure 5a, the contact time significantly impacts RhB dye sorption onto $MgTiO_3@g\text{-}C_3N_4$. For all concentrations, adsorption capacity increases progressively with the contact time until 40 min, when it attains equilibrium. Two well-known kinetic models were used to explain the RhB adsorption kinetics on $MgTiO_3@g\text{-}C_3N_4$. The original nonlinearized forms of the pseudo-first-order (Equation (1)) and pseudo-second-order (Equation (2)), and the Elovich (Equation (3)) kinetic models were utilized [47,48].

$$q_t = q_e\left(1 - \exp^{-K_1 . t}\right) \tag{1}$$

$$q_t = \frac{k_2 . q_e^2 . t}{1 + k_2 . q_e . t} \tag{2}$$

$$qt = 1\,\beta\,\ln(1 + \alpha\beta t) \tag{3}$$

where k_1 (min^{-1}) and k_2 (g mg^{-1} min^{-1}) are the rate constants of the pseudo-first-order and the pseudo-second-order, accordingly; q_t (mg g^{-1}) is the adsorption capacities displayed by the adsorbent at time t, and q_e is q_t at equilibrium; α (mmol g^{-1} s^{-1}) is the initial rate sorption, and β (g mmol^{-1}) is the sorption constant. Figure 5b–d demonstrates the pseudo-first-order, pseudo-second-order, and Elovich investigations for the RhB sorption onto $MgTiO_3@g\text{-}C_3N_4$, and the kinetic findings were gathered in Table 1. The RhB sorption on $MgTiO_3@g\text{-}C_3N_4$ fitted to the pseudo-second-order with an R^2 value of 1.000, and the computed q_e was almost typical of the experimental one.
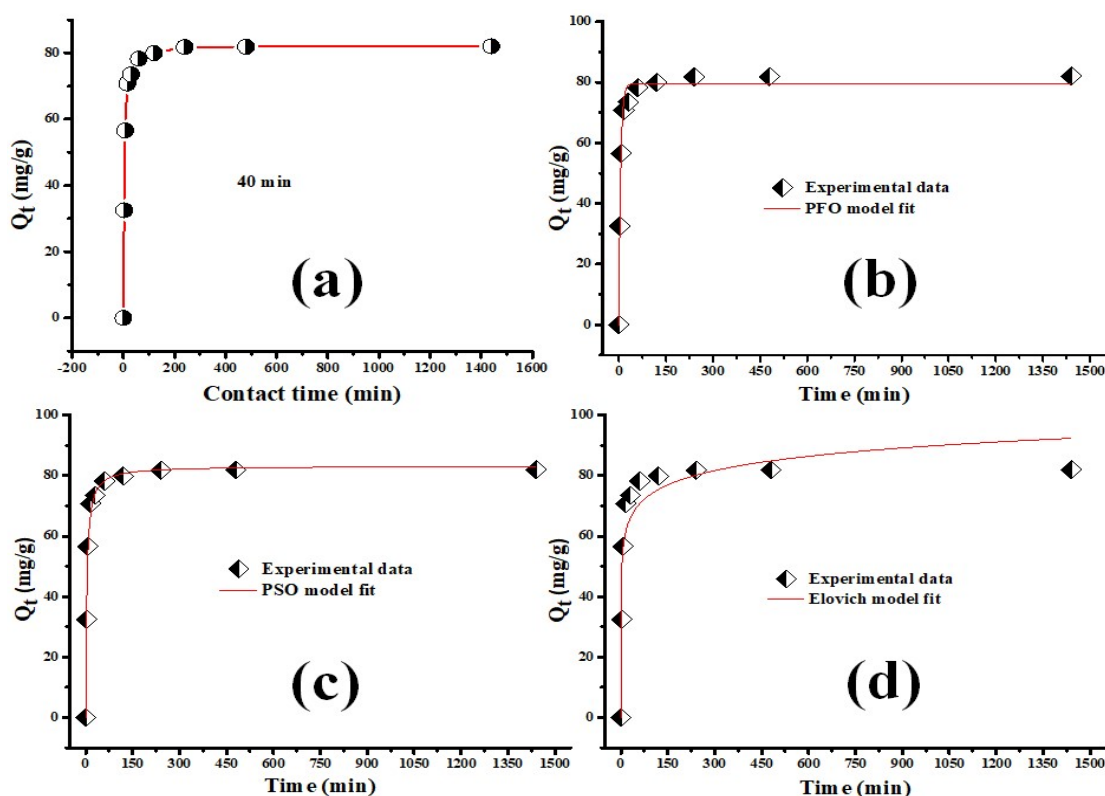
Figure 5. (**a**) The contact time study, (**b**–**d**) kinetic investigation of RhB sorption on MgTiO$_3$@g-C$_3$N$_4$ nanohybrid via the pseudo-first-order model, pseudo-second-order model, and Elovich model, respectively.

Table 1. Kinetic model parameters for the adsorption of RhB dye by nanocomposite.

	Pseudo-First-Order Model			Elovich Model		
	q$_e$(Cal)[b] (mg g^{-1})	K$_1$ × 10^3 (min^{-1})	r^2	β × 10^2 (g mg^{-1})	α	r^2
RhB	16.96	4.63	0.5701	0.241	3.79 × 10^6	0.7310
	Pseudo-Second-Order Model					
RhB	q$_e$ (Exp)[a] (mg g^{-1})	t$_{1/2}$ (min)	h$_0$ (mg g^{-1}.min^{-1})	q$_{e(Cal)}$ [b] (mg g^{-1})	K$_2$ × 10^3 (g mg^{-1} min^{-1})	r^2
	85	2.99	27.48	82.24	4.06	1.000

2.2.3. Intra-Particle Diffusion Study for Nanohybrid

The intraparticle diffusion model (IPDM) was utilized to investigate the RB sorption mechanism onto the MgTiO$_3$@g-C$_3$N$_4$ nanohybrid. According to Equation (6), the obtained q_t plot against the $t^{1/2}$ is monitored in Figure 4.

$$q_t = K_{ip} * t^{\frac{1}{2}} + C_i \tag{4}$$

K_{ip} (mg g^{-1} min$^{-0.5}$) represents the rate constant of the IPDM, and C (arbitrary) is a constant proportional to the boundary-layer thickness [49]. Obtaining a C value of zero (i.e., the line pass through the origin point) indicated that IPDM controlled the RB sorption, which is not the case here (Table 2). Thus, Figure 6 revealed three linear regressions, illustrating that the IPDM was participating but not the only mechanism controlling the RhB sorption on the MgTiO$_3$@g-C$_3$N$_4$ nanohybrid [50].

Table 2. Adsorption rate control mechanism parameters for removing RhB by MgTiO$_3$@g-C$_3$N$_4$ nanohybrid.

Intra-Particle Diffusion/Transport Model								
k_{dif} (mg.g^{-1} min$^{-1/2}$)	C1	r^2	k_{dif} (mg g^{-1} min$^{-1/2}$)	C2	r^2	k_{dif} (mg g^{-1} min$^{-1/2}$)	C3	r^2
17.5340	5.06	0.9603	0.4543	74.82	0.9940	0.0093	81.66	0.9838
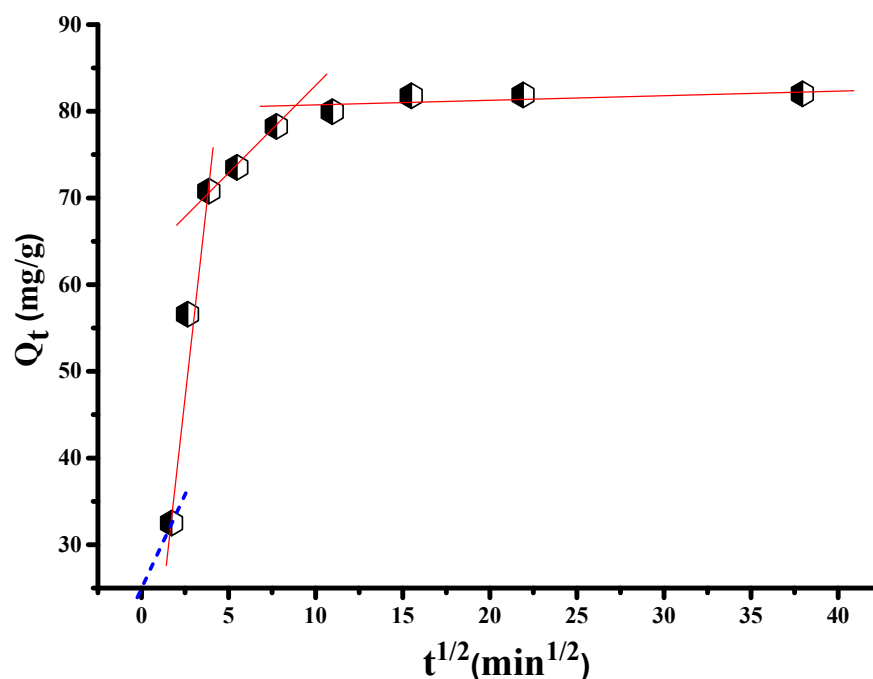
Figure 6. Adsorption mechanism investigation for removing RhB by MgTiO$_3$@g-C$_3$N$_4$ nanohybrid via the intraparticle diffusion model.

2.2.4. MgTiO$_3$@g-C$_3$N$_4$ Nanohybrids Adsorption Isotherm

In order to provide insight into sorbent-sorbate interactions, the equilibrium data of RhB sorption onto MgTiO$_3$@g-C$_3$N$_4$ at 25 °C was treated via isotherm models. Specifically, the Langmuir (LIM, Equation (5)), Fredulich (FIM, Equation (6)), and Temkin (TIM, Equation (7)) isotherm models were selected to investigate sorption possibilities [34,51,52].

$$\frac{1}{q_e} = \frac{1}{K_l \, q_m} \cdot \frac{1}{C_e} + \frac{1}{K_l} \tag{5}$$

$$\ln q_e = \ln K_f + \frac{1}{n} \ln C_e \tag{6}$$

$$q_e = \frac{RT}{b_T} \ln A_T + \frac{R_T}{b_T} \ln C_e \tag{7}$$

where q_m (mg g^{-1}) is the computed maximum q_t, K_L (L mg^{-1}) and K_f (L mg^{-1}) are Langmuir and Freundlich constants, respectively, and relate to sorption energy change and sorbent's capacity, respectively; while n is the Freundlich constant related to sorption's favorability. A_T (L mg^{-1}) and b_T (J mol^{-1}) are the TIM constant and Temkin constant associated with the heat of sorption. Figure 7 illustrates the linear and nonlinear plots of LIM, FIM, and TIM. The isotherms result (Table 3) indicated that the RhB sorption by MgTiO$_3$@g-C$_3$N$_4$ fitted LIM with an R^2 of 0.999. In addition, the 1/n value of less than one implied the favorability of RhB sorption on MgTiO$_3$@g-C$_3$N$_4$ [52]. Temkin's correlation coefficient suggested an essential role for electrostatic interaction in the sorption mechanism [53].
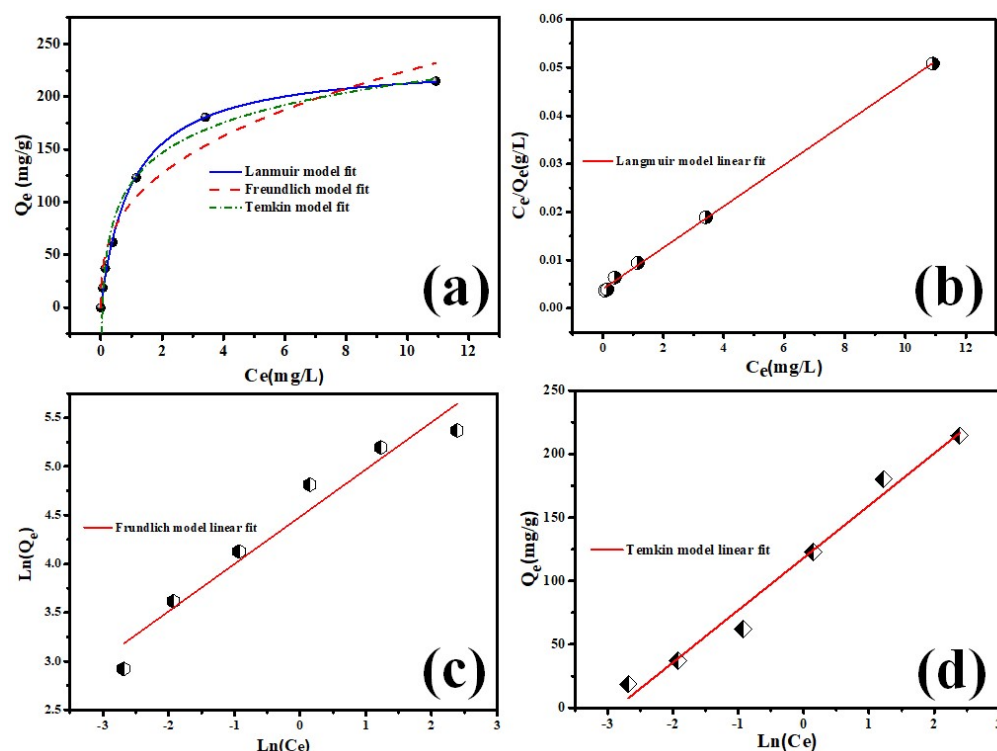
Figure 7. Isotherm investigation for RhB sorption on $MgTiO_3@g$-C_3N_4 using (**a**) Nonlinear LIM, FIM, and TIM; (**b**) Linearized LIM; (**c**) Linearized FIM; (**d**) Linearized TIM.

Table 3. Different equilibrium Isotherms' constants for RhB dye adsorption by $MgTiO_3$-g-C_3N_4 nanomaterial.

Equilibrium Model	Parameters	RhB
Langmuir	q_m (mg.g^{-1})	232.02
	K_L (mg.g^{-1})	0.0047
	R_L (L.mg^{-1})	0.4788
	R^2	0.9991
Freundlich	n	2.06
	K_F (L.mg^{-1})	88.64
	R^2	96488
Temkin	B (J.mol^{-1})	60.18
	K_T (L.mg^{-1})	17.65
	R^2	0.9816

2.2.5. RhB Dye Adsorption Mechanism

To comprehend the adsorption process, FTIR spectra (Figure 8a,b) of $MgTiO_3@g$-C_3N_4 nanohybrid before and after the adsorption of RhB dye were recorded in the region of 400–3600 cm^{-1}. The FTIR spectrum of the nanohybrid $MgTiO_3@g$-C_3N_4 is broad between 3000 and 3400 cm^{-1} due to the stretching modes of the O–H and terminal amino groups. The bands at 1232, 1315, and 1454 cm^{-1} correspond to aromatic C–N stretching, whereas the peaks at 1574 and 1632 cm^{-1} correspond to C≡N stretching. The band at 892 cm^{-1} corresponds to the triazine ring mode peak, which is a typical mode in carbon nitride. As demonstrated in Figure 8a, the FTIR spectrum of $MgTiO_3@g$-C_3N_4 nanohybrid shifted slightly after RhB dye adsorption. Furthermore, the central peak in the broadband at 3165 cm^{-1} changed to 3157, revealing that the OH and amino groups of $MgTiO_3@g$-C_3N_4 nanohybrid were entangled throughout the adsorption process. This observed result could be caused by the interaction between RhB molecules and $MgTiO_3@g$-C_3N_4 nanohybrid hydrogen bonds. In addition, a vibrational triazine ring mode at 888 cm^{-1} nearly shifted with the adsorption of RhB dye,

which was attributed to the π-π interaction between the electron clouds in the g-C$_3$N$_4$ skeleton of MgTiO$_3$@g-C$_3$N$_4$ nanohybrid and the aromatic rings of RhB molecules. Consequently, as depicted in Figure 8b, RhB dye molecules are adsorbed onto the MgTiO$_3$@g-C$_3$N$_4$ nanohybrid. On the nanohybrid, the hydrogen bonds and π-π interactions enhance the adsorption of RhB dyes. The contact time trend (Figure 5a) may be deduced from the surface area reducing after the pores have filled. Furthermore, the agreement of sorption to the FIM may explain the slowdown in the sorption rate after the first hour.
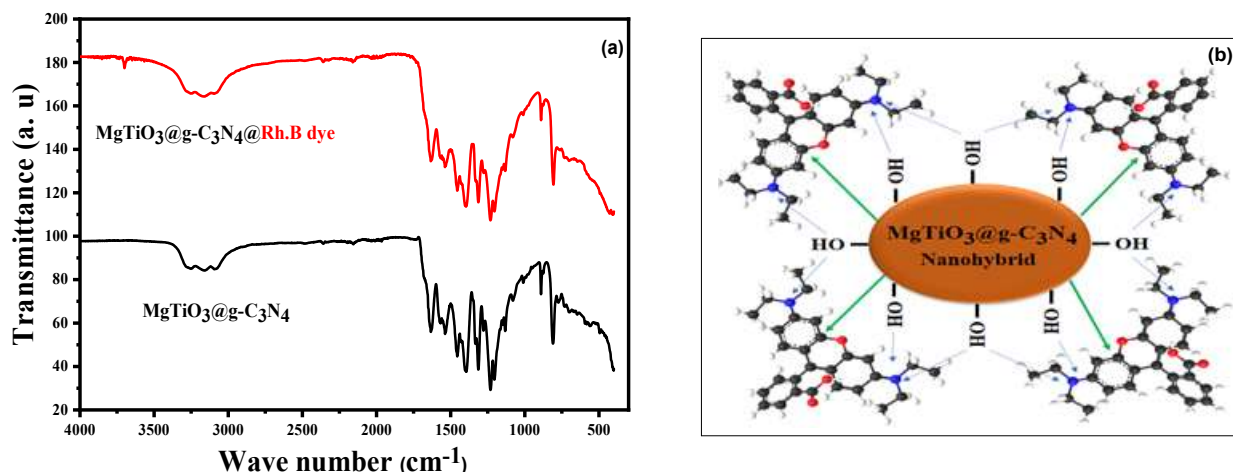
Figure 8. FTIR spectra of (**a**) MgTiO$_3$@g-C$_3$N$_4$@RhB before and after adsorption, and (**b**) proposed adsorption mechanism.

2.3. MgTiO$_3$@g-C$_3$N$_4$ Nanohybrid Regeneration

The regeneration capacity of the hybrid was examined by eliminating the RhB dye from the MgTiO$_3$@g-C$_3$N$_4$ nanohybrid. The ethanol solvent demonstrated the desorption of RhB dye from the MgTiO$_3$@g-C$_3$N$_4$ nanohybrid instantaneous coloring. The freshly generated RhB dye solution's volume and concentration were then applied to the MgTiO$_3$@g-C$_3$N$_4$ nanohybrid (25 mg/L, 100 mL). Five times this entire cycle was repeated. The removal effectiveness of the RhB dye from MgTiO$_3$@g-C$_3$N$_4$ nanohybrid desorbed by ethanol and distilled water is given in (Figure 9). With each desorption cycle, it was found that the MgTiO$_3$@g-C$_3$N$_4$ nanohybrid's ability to remove dyes somewhat diminished.
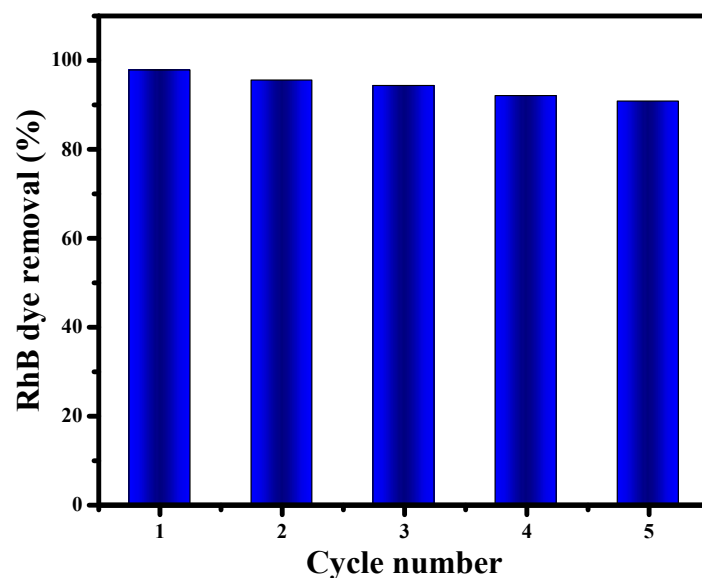
Figure 9. Reuse investigations for the regenerated MgTiO$_3$@g-C$_3$N$_4$ in removing RhB.

2.4. Adsorption Capability of MgTiO_3@g-C_3N_4 Nanohybrids for other Color Contaminants

To test the adsorption capability of MgTiO$_3$@g-C$_3$N$_4$ nanohybrid, various dye solutions with fixed concentrations (50 mg/L) were studied. Extraction tests were conducted by combining the obtained MgTiO$_3$@g-C$_3$N$_4$ nanohybrid sorbent (10 mg) with dyes and an aqueous solution (25 mL), in a 50 mL bottle for 24 h at room temperature with magnetic stirring. After centrifuging the dye solutions for 10 min, 5.0 mL of the supernatant solutions recovered. The capacity of MgTiO$_3$@g-C$_3$N$_4$ nanohybrid to adsorb various colors from an aqueous solution was evaluated. Figure 10 depicts the removal percentage of various dyes by MgTiO$_3$@g-C$_3$N$_4$ nanohybrid adsorbent. The obtained results confirmed that the elimination ability percentages of malachite green (MG), methylene blue (MB), indigo carmine (IC), crystal violet (CV), congo red (CR), and basic fuchsin (BF) were 93, 99, 87, 95, 96, and 87%, respectively. However, the uptake of MB and CR dyes was higher than that of other colors.
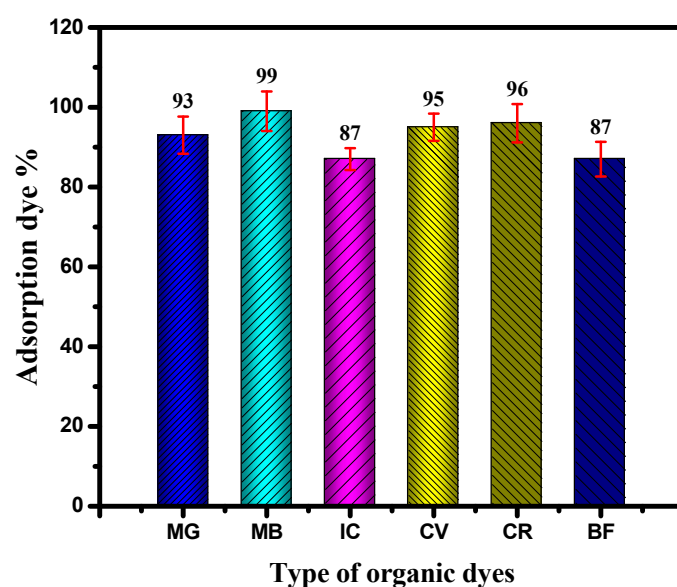
Figure 10. Applicability of MgTiO$_3$@g-C$_3$N$_4$ for removing other organic contaminants from water.

Compared to recent literature findings, MgTiO$_3$@g-C$_3$N$_4$ nanohybrid performed competitively under optimized operating conditions in removing RB within 40 min (Table 4). This finding can be attributed to the high surface area of 107 m^2 g^{-1} and the mesoporous material nature of this sorbent. In addition to removing toxic metals and organic pollutants, this nanomaterial is also cost-effective.

Table 4. Recent literature findings compared to the MgTiO$_3$@g-C$_3$N$_4$ fabricated in this study in removing RhB.

Nanomaterial	Adsorption Capacity (mg. g^{-1})	Reference
MgTiO$_3$@g-C$_3$N$_4$ nanohybrids	223	This study
Carbon microspheres	19.9	[54]
Fe$_2$O$_4$-montmorillonite nanocomposite	209	[55]
Zn–Fe layered double hydroxide-activated carbon nanocomposite	97.0	[56]
Activated carbon	264	[57]
Carbon–cobalt ferrite	94.1	[58]
activated carbon-supported MgO/MnO$_2$	16.2	[59]

3. Experimental Section

3.1. Building Up of MgTiO$_3$@g-C$_3$N$_4$ Nanomaterials

The powdered g-C$_3$N$_4$ was produced through the decomposition of the urea compound. An amount of 7 g of urea substance was loaded in a covered pot and heated at 550 °C for 2.0 h. The acquired raw, yellow g-C$_3$N$_4$ was then allowed to cool, ground, and packed into a bottle. Magnesium oxide (MgO) powder was produced by the thermal degradation of MgCO$_3$ in a muffle furnace (SNOL-LSF21) at 800 °C for 1.0 h, whereas nanosized TiO$_2$ was purchased from Sigma Aldrich. Using a standard ultrasonication procedure (Ultrasonic cleaner-100W, Labtech-Co., LTD, Seol, Korea), MgTiO$_3$@g-C$_3$N$_4$ nanomaterial was fabricated. In 125 mL of methanol, 1.84 g of g-C$_3$N$_4$ was ultrasonically treated for 15 min. The g-C$_3$N$_4$ in methanol solution received 400 mg of MgO and TiO$_2$ nanopowder, which was then sonicated for an extra 45 min. The resultant yellowish solution was heated at 85 °C for 24.0 h and 180 °C for 1.0 h; then the produced MgTiO$_3$@g-C$_3$N$_4$ nanomaterial was annealed.

3.2. Characterization

The prepared MgTiO$_3$@g-C$_3$N$_4$ nanohybrid was characterized using X-ray Diffraction (XRD) (PAN-alytical X'Pert Pro Multipurpose Diffractometer), Cu-Kα X-ray radiation (λ = 1.5418 Å) at 40 kV and a current 5.0 flow of 40 mA. The structure, surface morphology, and elemental characterization of the MgTiO$_3$@g-C$_3$N$_4$ nanohybrid were determined by using Field emission scanning electron microscope (FESEM) and Energy-dispersive X-ray spectroscopy (EDX) techniques, respectively (FESEM Carl Zeiss Merlin Compact, Oberkochen, Germany). The specific surface area of MgTiO$_3$@g-C$_3$N$_4$ nanohybrid was measured using the BET (Brunauer-Emmett-Teller) analyzer (Micrometrics ASAP 2020, Miami, FL, USA) using the N$_2$ adsorption-desorption method, where a sample was dried under a constant flow of N$_2$ at 60 °C for 24 h. TEM images were acquired using FEI Tecnai G2 20 TWIN microscope (Miami, FL, USA) operating at 200 kV. The salt addition method evaluated the point of zero charges (pHpzc). The Fourier Transform Infra-Red (FTIR) spectrum was recorded to determine the existence of functional groups present over the surface of the adsorbent by using FTIR (Shimadzu IR AFFINITY-I, Tokyo, Japan).

3.3. RhB Dye Removal Experiments

Dye adsorption tests were conducted in Erlenmeyer flasks in batch mode; an adsorbent dosage of 0.01 g of MgTiO$_3$@g-C$_3$N$_4$ nanohybrid was used to remove RhB dye from 25 mL solutions containing 25 to 100 mg/L of the dye. To attain the required dye concentrations, the dye stock solutions (1000 mg/L) were diluted with three times as much distilled water for all adsorption studies. All studies were conducted in the dark using an orbital shaker at 272 °C and 180 rpm shaking speed. Adjusting the pH of the dye solution with (0.1 M) HCl and (0.1 M) NaOH solution. Utilizing a UV-VIS spectrophotometer, the concentration of the dye solutions was measured (UV-1800 Spectrophotometer Shimadzu). A duration of 15 min was used to remove the MgTiO$_3$@g-C$_3$N$_4$ nanohybrid from the dye solution using centrifugation at 5000× *g* rpm. The absorbance values of the supernatant were measured to determine the remaining RhB dye concentration at a wavelength (λ max) of 550 nm. Employing the following expression, the adsorption capacity of the MgTiO$_3$@g-C$_3$N$_4$ nanohybrid for the removal of RhB dye and the removal % was calculated:

$$Q_e = w \times \frac{(C_0 - C_e)}{V} \tag{8}$$

$$RhB \text{ removal } (\%) = 100 \times \frac{(C_0 - C_e)}{C_0} \tag{9}$$

3.4. Regeneration Experiments

Methanol and distilled water have been investigated as desorbing solutions for MgTiO$_3$@g-C$_3$N$_4$ nanohybrid regeneration investigations for RhB dye. Under ideal condi-

tions, 25 mg/L concentrations of the RhB dye in 100 mL volumes were initially adsorbed onto the MgTiO$_3$@g-C$_3$N$_4$ nanohybrid. After that, centrifugation was used to remove the solution from the used MgTiO$_3$@g-C$_3$N$_4$ nanohybrid. Next, the separated MgTiO$_3$@g-C$_3$N$_4$ nanohybrid was submerged in 50 mL of methanol and 50 mL of distilled water, each for 60 min, in an orbital shaker. The MgTiO$_3$@g-C$_3$N$_4$ nanohybrid was then washed three times with deionized water and oven dried to assess their reusability. Using ethanol and distilled water solution, the MgTiO$_3$@g-C$_3$N$_4$ nanohybrid's efficiency for reuse in up to five cycles was calculated.

4. Conclusions

In this study, MgTiO$_3$@g-C$_3$N$_4$ nanohybrids were used as adsorbents to remove the hazardous RhB dye. By combining MgO, TiO$_2$, and g-C$_3$N$_4$ nanosheets, MgTiO$_3$@g-C$_3$N$_4$ nanohybrids were fabricated. The synthesized composite possessed adsorption capabilities of 232 mg/g and a strong correlation coefficient. RhB adsorption was well represented by the Langmuir isotherm model and followed pseudo-second-order kinetics. The relevance of electrostatic interaction, hydrogen bonding, and π-π interaction between the dye molecules and MgTiO$_3$@g-C$_3$N$_4$ nanohybrids was proposed by FTIR analyses of the adsorption mechanism. In addition to having a broader range of applications, the composite was successful in removing other dyes. Thus, the present work demonstrates that MgTiO$_3$@g-C$_3$N$_4$ nanohybrids, with their excellent adsorption efficiencies, are highly important for eliminating polluted colors.

Author Contributions: A.M.: Conceptualization, writing original draft, preparation; M.R.E.: Supervision, writing, review the final version; B.Y.A.: Writing, review the final version; N.Y.E.: Validation, writing, review; H.I.: Writing, review; F.A.A.: Writing, review; A.E.A.: Review. All authors have read and agreed to the published version of the manuscript.

Conflicts of Interest: The authors declare that they have no known competing financial interests or personal relationships that could have appeared to influence the work reported in this paper.

References

1. Wu, C.; Maurer, C.; Wang, Y.; Xue, S.; Davis, D.L. Water pollution and human health in China. *Environ. Health Perspect.* **1999**, *107*, 251–256. [CrossRef] [PubMed]
2. Elamin, M.R.; Abdulkhair, B.Y.; Elzupir, A.O. Removal of ciprofloxacin and indigo carmine from water by carbon nanotubes fabricated from a low-cost precursor: Solution parameters and recyclability. *Ain Shams Eng. J.* **2023**, *14*, 101844. [CrossRef]
3. Bhattacharjee, R.; Mitra, T.; Mitra, P.; Biswas, S.; Ghosh, S.; Chattopadhyay, S.; Malik, S.; Dey, A. Effective Materials in the Photocatalytic Treatment of Dyestuffs and Stained Wastewater. In *Trends and Contemporary Technologies for Photocatalytic Degradation of Dyes*; Springer: Berlin/Heidelberg, Germany, 2022; pp. 173–200.
4. Idriss, H. Decolorization of malachite green in aqueous solution via MgO nanopowder. *J. Optoelectron. Biomed. Mater. Vol.* **2021**, *13*, 183–192.
5. Elamin, M.R.; Ibnaouf, K.H.; Elamin, N.Y.; Adam, F.A.; Alolayan, A.H.; Abdulkhair, B.Y. Spontaneous Adsorption and Efficient Photodegradation of Indigo Carmine under Visible Light by Bismuth Oxyiodide Nanoparticles Fabricated Entirely at Room Temperature. *Inorganics* **2022**, *10*, 65. [CrossRef]
6. Farnum, J.L. Examining the Effects of Synthetic Dye Yellow No. 5 (Tartrazine) Exposure on Mouse Neuro2A Neurons In Vitro. Bachelor's Thesis, University of Central Florida, Orlando, FL, USA, 2022.
7. Adam, F.A.; Ghoniem, M.; Diawara, M.; Rahali, S.; Abdulkhair, B.Y.; Elamin, M.; Aissa, M.A.B.; Seydou, M. Enhanced adsorptive removal of indigo carmine dye by bismuth oxide doped MgO based adsorbents from aqueous solution: Equilibrium, kinetic and computational studies. *RSC Adv.* **2022**, *12*, 24786–24803. [CrossRef]
8. Almufarij, R.S.; Abdulkhair, B.Y.; Salih, M.; Aldosari, H.; Aldayel, N.W. Optimization, Nature, and Mechanism Investigations for the Adsorption of Ciprofloxacin and Malachite Green onto Carbon Nanoparticles Derived from Low-Cost Precursor via a Green Route. *Molecules* **2022**, *27*, 4577. [CrossRef]
9. Yusuf, T.L.; Orimolade, B.O.; Masekela, D.; Mamba, B.; Mabuba, N. The application of photoelectrocatalysis in the degradation of rhodamine B in aqueous solutions: A review. *RSC Adv.* **2022**, *12*, 26176–26191. [CrossRef]
10. Saigl, Z.M. Various Adsorbents for Removal of Rhodamine B Dye: A Review. *Indones. J. Chem.* **2021**, *21*, 1039–1056. [CrossRef]

11. Al-Gheethi, A.A.; Azhar, Q.M.; Kumar, P.S.; Yusuf, A.A.; Al-Buriahi, A.K.; Mohamed, R.M.S.R.; Al-Shaibani, M.M. Sustainable approaches for removing Rhodamine B dye using agricultural waste adsorbents: A review. *Chemosphere* **2022**, *287*, 132080. [CrossRef]

12. Kong, Y.; Wang, M.; Lu, W.; Li, L.; Li, J.; Chen, M.; Wang, Q.; Qin, G.; Cao, D. Rhodamine-based chemosensor for Sn^{2+} detection and its application in nanofibrous film and bioimaging. *Anal. Bioanal. Chem.* **2022**, *414*, 2009–2019. [CrossRef]

13. Saravanan, S.; Kumar, P.S.; Chitra, B.; Rangasamy, G. Biodegradation of textile dye Rhodamine-B by Brevundimonas diminuta and screening of their breakdown metabolites. *Chemosphere* **2022**, *308*, 136266. [CrossRef] [PubMed]

14. Manohar, M.; Paladhi, A.G.; Jacob, S.; Vallinayagam, S. ZnO Nanocomposites in Dye Degradation. In *Advanced Oxidation Processes in Dye-Containing Wastewater*; Springer: Berlin/Heidelberg, Germany, 2022; pp. 317–341.

15. Ranjan Mishra, S.; Gadore, V.; Ahmaruzzaman, M. Nanostructured Composite Materials for Treatment of Dye Contaminated Water. In *Nanohybrid Materials for Water Purification*; Springer: Berlin/Heidelberg, Germany, 2022; pp. 97–120.

16. Birniwa, A.H.; Abubakar, A.S.; Mahmud, H.N.M.E.; Kutty, S.R.M.; Jagaba, A.H.; Abdullahi, S.S.A.; Zango, Z.U. Application of Agricultural Wastes for Cationic Dyes Removal from Wastewater. In *Textile Wastewater Treatment*; Springer: Berlin/Heidelberg, Germany, 2022; pp. 239–274.

17. Sengupta, A.; Sarkar, A. Green synthesis of nanoparticles: Prospect for sustainable efficient photocatalytic dye degradation. In *Photocatalytic Degradation of Dyes*; Elsevier: Amsterdam, The Netherlands, 2021; pp. 405–420.

18. Ntakadzeni, M. Molybdenum Sulfide Nanostructures: Synthesis and Their Catalytic Applications. Ph.D. Thesis, University of Johannesburg (South Africa), Johannesburg, South Africa, 2017.

19. Skjolding, L.M.; Dyhr, K.; Köppl, C.; McKnight, U.; Bauer-Gottwein, P.; Mayer, P.; Bjerg, P.; Baun, A. Assessing the aquatic toxicity and environmental safety of tracer compounds Rhodamine B and Rhodamine WT. *Water Res.* **2021**, *197*, 117109. [CrossRef] [PubMed]

20. Shindhal, T.; Rakholiya, P.; Varjani, S.; Pandey, A.; Ngo, H.H.; Guo, W.; Ng, H.Y.; Taherzadeh, M.J. A critical review on advances in the practices and perspectives for the treatment of dye industry wastewater. *Bioengineered* **2021**, *12*, 70–87. [CrossRef] [PubMed]

21. Saravanan, A.; Kumar, P.S.; Jeevanantham, S.; Karishma, S.; Tajsabreen, B.; Yaashikaa, P.; Reshma, B. Effective water/wastewater treatment methodologies for toxic pollutants removal: Processes and applications towards sustainable development. *Chemosphere* **2021**, *280*, 130595. [CrossRef]

22. Rathi, B.S.; Kumar, P.S. Application of adsorption process for effective removal of emerging contaminants from water and wastewater. *Environ. Pollut.* **2021**, *280*, 116995. [CrossRef]

23. Shamsudin, R. Kenaf Bast Fiber Filter Cartridge for Removal of Heavy Metals and Dyes in Aqueous Solution. Ph.D. Thesis, Universiti Pendidikan Sultan Idris, Tanjung Malim, Malaysia, 2016.

24. Rashed, M.N. Adsorption technique for the removal of organic pollutants from water and wastewater. *Org. Pollut.-Monit. Risk Treat.* **2013**, *7*, 167–194.

25. Elamin, M.R.; Abdulkhair, B.Y.; Elzupir, A.O. Insight to aspirin sorption behavior on carbon nanotubes from aqueous solution: Thermodynamics, kinetics, influence of functionalization and solution parameters. *Sci. Rep.* **2019**, *9*, 12795. [CrossRef]

26. Elamin, M.R.; Elzupir, A.O.; Abdulkhair, B.Y. Monitoring; Management. Synthesis and characterization of functionalized carbon nanofibers for efficient removal of highly water-soluble dextromethorphan and guaifenesin from environmental water samples. *Environ. Nanotechnol. Monit. Manag.* **2021**, *15*, 100397.

27. Shi, C.; Yu, S.; Wang, L.; Zhang, X.; Lin, X.; Li, C. Degradation of tetracycline/oxytetracycline by electrospun aligned polyacrylonitrile-based carbon nanofibers as anodic electrocatalysis microfiltration membrane. *J. Environ. Chem. Eng.* **2021**, *9*, 106540. [CrossRef]

28. Zhou, Y.; Lu, J.; Zhou, Y.; Liu, Y. Recent advances for dyes removal using novel adsorbents: A review. *Environ. Pollut.* **2019**, *252*, 352–365. [CrossRef]

29. Moosavi, S.; Lai, C.W.; Gan, S.; Zamiri, G.; Akbarzadeh Pivehzhani, O.; Johan, M.R. Application of efficient magnetic particles and activated carbon for dye removal from wastewater. *ACS Omega* **2020**, *5*, 20684–20697. [CrossRef] [PubMed]

30. Sahoo, T.R.; Prelot, B. Adsorption processes for the removal of contaminants from wastewater: The perspective role of nanomaterials and nanotechnology. In *Nanomaterials for the Detection and Removal of Wastewater Pollutants*; Elsevier: Amsterdam, The Netherlands, 2020; pp. 161–222.

31. Mary, B.C.J.; Vijaya, J.J.; Bououdina, M.; Khezami, L.; Modwi, A.; Ismail, M.; Bellucci, S. On this page. *Adsorpt. Sci. Technol.* **2022**, *2*, 3.

32. Al-Awaji, N.; Boukriba, M.; Albadri, A.; Aissa, M.A.B.; Bououdina, M.; Modwi, A. Green Ca-Loaded MgO Nanoparticles as an Efficient Adsorbent for Organic Hazardous Dyes. *J. Nanomater.* **2022**, *2022*, 5062752. [CrossRef]

33. Ali, M.; Modwi, A.; Idriss, H.; Aldaghri, O.; Ismail, M.; Ibnaouf, K. Detoxification of Pb (II) from aquatic media via CaMgO$_2$@ g-C$_3$N$_4$ nanocomposite. *Mater. Lett.* **2022**, *322*, 132501. [CrossRef]

34. Aldaghri, O.; Modwi, A.; Idriss, H.; Ali, M.; Ibnaouf, K. Cleanup of Cd II from water media using Y2O3@ gC3N4 (YGCN) nanocomposite. *Diam. Relat. Mater.* **2022**, *129*, 109315. [CrossRef]

35. Khezami, L.; Aissa, M.A.B.; Modwi, A.; Ismail, M.; Guesmi, A.; Algethami, F.K.; Ticha, M.B.; Assadi, A.A.; Nguyen-Tri, P. Harmonizing the photocatalytic activity of g-C3N4 nanosheets by ZrO$_2$ stuffing: From fabrication to experimental study for the wastewater treatment. *Biochem. Eng. J.* **2022**, *182*, 108411. [CrossRef]

36. Modwi, A.; Khezami, L.; Ghoniem, M.; Nguyen-Tri, P.; Baaloudj, O.; Guesmi, A.; AlGethami, F.; Amer, M.; Assadi, A. Superior removal of dyes by mesoporous MgO/g-C$_3$N$_4$ fabricated through ultrasound method: Adsorption mechanism and process modeling. *Environ. Res.* **2022**, *205*, 112543. [CrossRef]

37. Yu, Y.; Yan, W.; Wang, X.; Li, P.; Gao, W.; Zou, H.; Wu, S.; Ding, K. Surface engineering for extremely enhanced charge separation and photocatalytic hydrogen evolution on g-C$_3$N$_4$. *Adv. Mater.* **2018**, *30*, 1705060. [CrossRef]

38. Wu, Z.; He, X.; Gao, Z.; Xue, Y.; Chen, X.; Zhang, L. Synthesis and characterization of Ni-doped anatase TiO$_2$ loaded on magnetic activated carbon for rapidly removing triphenylmethane dyes. *Environ. Sci. Pollut. Res.* **2021**, *28*, 3475–3483. [CrossRef]

39. Vesali-Kermani, E.; Habibi-Yangjeh, A.; Ghosh, S. Visible-light-induced nitrogen photofixation ability of g-C$_3$N$_4$ nanosheets decorated with MgO nanoparticles. *J. Ind. Eng. Chem.* **2020**, *84*, 185–195. [CrossRef]

40. Yue, Y.; Zhang, P.; Wang, W.; Cai, Y.; Tan, F.; Wang, X.; Qiao, X.; Wong, P.K. Enhanced dark adsorption and visible-light-driven photocatalytic properties of narrower-band-gap Cu$_2$S decorated Cu$_2$O nanocomposites for efficient removal of organic pollutants. *J. Hazard. Mater.* **2020**, *384*, 121302. [CrossRef] [PubMed]

41. Modwi, A.; Abbo, M.; Hassan, E.; Houas, A. Effect of annealing on physicochemical and photocatalytic activity of Cu 5% loading on ZnO synthesized by sol–gel method. *J. Mater. Sci. Mater. Electron.* **2016**, *27*, 12974–12984. [CrossRef]

42. Li, Y.; Lv, K.; Ho, W.; Dong, F.; Wu, X.; Xia, Y. Hybridization of rutile TiO$_2$ (rTiO$_2$) with g-C$_3$N$_4$ quantum dots (CN QDs): An efficient visible-light-driven Z-scheme hybridized photocatalyst. *Appl. Catal. B Environ.* **2017**, *202*, 611–619. [CrossRef]

43. Tella, E.; Panagiotou, G.; Petsi, T.; Bourikas, K.; Kordulis, C.; Lycourghiotis, A. The mechanism of retention of vanadium oxo-species at the "titanium oxide/aqueous solution" interface. *Glob NEST J.* **2010**, *12*, 231–238.

44. Cardenas Peña, A.M.; Ibáñez Cornejo, J.G.; Vásquez Medrano, R.C. *Determination of the Point of Zero Charge for Electrocoagulation Precipitates from an Iron Anode*; Universidad Iberoamericana: Mexico City, Mexico, 2012.

45. Nasiruddin Khan, M.; Sarwar, A. Determination of points of zero charge of natural and treated adsorbents. *Surf. Rev. Lett.* **2007**, *14*, 461–469. [CrossRef]

46. Mahmood, T.; Saddique, M.T.; Naeem, A.; Westerhoff, P.; Mustafa, S.; Alum, A. Comparison of different methods for the point of zero charge determination of NiO. *Ind. Eng. Chem. Res.* **2011**, *50*, 10017–10023. [CrossRef]

47. Elamin, M.R.; Abdulkhair, B.Y.; Algethami, F.K.; Khezami, L. Linear and nonlinear investigations for the adsorption of paracetamol and metformin from water on acid-treated clay. *Sci. Rep.* **2021**, *11*, 13606. [CrossRef]

48. Guarín Romero, J.R.; Moreno-Piraján, J.C.; Giraldo Gutierrez, L. Kinetic and equilibrium study of the adsorption of CO2 in ultramicropores of resorcinol-formaldehyde aerogels obtained in acidic and basic medium. *C* **2018**, *4*, 52. [CrossRef]

49. An, B. Cu (II) and As (V) adsorption kinetic characteristic of the multifunctional amino groups in chitosan. *Processes* **2020**, *8*, 1194. [CrossRef]

50. Ho, Y.; McKay, G. The kinetics of sorption of basic dyes from aqueous solution by sphagnum moss peat. *Can. J. Chem. Eng.* **1998**, *76*, 822–827. [CrossRef]

51. Al-Ghouti, M.A.; Da'ana, D.A. Guidelines for the use and interpretation of adsorption isotherm models: A review. *J. Hazard. Mater.* **2020**, *393*, 122383. [CrossRef] [PubMed]

52. Abdulkhair, B.Y.; Elamin, M.R. Low-Cost Carbon Nanoparticles for Removing Hazardous Organic Pollutants from Water: Complete Remediation Study and Multi-Use Investigation. *Inorganics* **2022**, *10*, 136. [CrossRef]

53. Liu, L.; Fan, S.; Li, Y. Removal behavior of methylene blue from aqueous solution by tea waste: Kinetics, isotherms and mechanism. *Int. J. Environ. Res. Public Health* **2018**, *15*, 1321. [CrossRef]

54. Saleh, T.A.; Ali, I. Synthesis of polyamide grafted carbon microspheres for removal of rhodamine B dye and heavy metals. *J. Environ. Chem. Eng.* **2018**, *6*, 5361–5368. [CrossRef]

55. Ouachtak, H.; El Haouti, R.; El Guerdaoui, A.; Haounati, R.; Amaterz, E.; Addi, A.A.; Akbal, F.; Taha, M.L. Experimental and molecular dynamics simulation study on the adsorption of Rhodamine B dye on magnetic montmorillonite composite γ-Fe$_2$O$_3$@ Mt. *J. Mol. Liq.* **2020**, *309*, 113142. [CrossRef]

56. Sirajudheen, P.; Meenakshi, S. Encapsulation of Zn–Fe layered double hydroxide on activated carbon and its litheness in tuning anionic and rhoda dyes through adsorption mechanism. *Asia-Pacific J. Chem. Eng.* **2020**, *15*, e2479. [CrossRef]

57. Albanio, I.I.; Muraro, P.C.L.; da Silva, W.L. Rhodamine B dye adsorption onto biochar from olive biomass waste. *Water Air Soil Pollut.* **2021**, *232*, 214. [CrossRef]

58. Hoang, L.P.; Van, H.T.; Nguyen, T.T.H.; Nguyen, V.Q.; Quang Thang, P. Coconut shell activated carbon/CoFe$_2$O$_4$ composite for the removal of rhodamine B from aqueous solution. *J. Chem.* **2020**, *2020*, 9187960. [CrossRef]

59. Yue, X.; Zhao, J.; Shi, H.; Chi, Y.; Salam, M. Preparation of composite adsorbents of activated carbon supported MgO/MnO$_2$ and adsorption of Rhodamine B. *Water Sci. Technol.* **2020**, *81*, 906–914. [CrossRef]